

# A phase field crystal theory of the kinematics and dynamics of dislocation lines

Vidar Skogvoll,<sup>1</sup> Luiza Angheluta,<sup>1</sup> Audun Skaugen,<sup>1</sup> Marco Salvalaglio,<sup>2,3</sup> and Jorge Viñals<sup>4</sup>

<sup>1</sup>*PoreLab, Njord Centre, Department of Physics,  
University of Oslo, P. O. Box 1048, 0316 Oslo, Norway*

<sup>2</sup>*Institute of Scientific Computing, TU Dresden, 01062 Dresden, Germany*

<sup>3</sup>*Dresden Center for Computational Materials Science (DCMS), TU Dresden, 01062 Dresden, Germany*

<sup>4</sup>*School of Physics and Astronomy, University of Minnesota, Minneapolis, MN 55455*

(Dated: October 8, 2021)

We present a general method to compute the dislocation density tensor and its evolution from the configuration of a spatially periodic order parameter associated with a given crystal symmetry. The method is applied to a phase field crystal model (PFC) of a bcc lattice, and used to investigate the shrinkage of a dislocation loop. The dislocation velocity is determined by the dynamics of the order parameter, and we have shown that the general expression predicts the overdamped motion induced by a Peach-Koehler force with mobilities determined by equilibrium properties. We introduce an additional, configuration dependent, lattice distortion, defined such that the configurational stress is maintained in elastic equilibrium at all times. The resulting far-field stress field agrees very well with predictions from continuum elasticity, while the near-field to defect core is regularized by lattice discreteness. For the shrinkage of a dislocation loop, we find that the classical PFC model captures its evolution only qualitatively, while the process happens on a much faster time scale when the system is constrained to remain in mechanical equilibrium. The formulation provides a robust and accurate tracking of defect motion in a deformed crystalline lattice.

## I. INTRODUCTION

The Phase Field Crystal (PFC) model is a widely used computational framework to describe non-equilibrium evolution of defected materials [1–3]. One of the strengths of the formulation is the ease in the description of complex material processes such as dislocation nucleation [4], dislocation dissociation and stacking fault formation [5], creep [6], fracture [7], and boundary driven grain motion [8–11]. The model amounts to a short-scale regularization of defect core divergences inherent in classical elasticity, while allowing for a consistent treatment of defect topology, dislocation cores, grain boundary structures, and associated mobilities. The only constitutive input required is the (defect free) equilibrium free energy of the lattice structure under study, without any additional specification of slip systems, stacking fault energies, or line or boundary mobilities. The PFC model begins with the definition of a scalar order parameter (or phase field)  $\psi(\mathbf{r}, t)$ , a function of space and time, so that its equilibrium configuration corresponds to a perfect, undistorted, crystal lattice. The non-convex free energy functional  $F[\psi]$  of the field and its gradients is chosen so that its minimizer has the same spatial symmetry as the lattice of interest [12]. The required free energies have been derived by using the methods of density functional theory [13–15], although our calculations below will rely on modified forms of the classical Brazovskii functional description of modulated phases [16], also known as the Swift-Hohenberg model in the convection literature [17]. Once the free energy functional is given, a kinetic law for the phase field is introduced which is conservative, relaxational in nature, and driven by free energy minimization.

Despite its successes to date, a precise formal relation

between the phase field crystal model as currently formulated and classical continuum plasticity theory has remained elusive [18]. The primary challenge is relating the continuous  $\psi$  phase field to the singular nature of crystal defects which is required in order to connect the PFC model with existing macroscopic plasticity theories [19, 20]. Progress was made in deriving this connection, albeit for the much simpler case of a two-dimensional (2D) isotropic system, in Ref. [21], in which the defects were identified as zeros of complex amplitudes associated with the base linear modes of the  $\psi$  phase field. In two dimensions, only edge dislocations are permitted, which are point defects, and the corresponding defect density is a vector field (the Burgers vector density). In three dimensions, one needs to consider one dimensional lines of singularity, and the corresponding defect density is the Nye dislocation density tensor,  $\alpha_{ij}$ , which permits both edge-, screw and mixed dislocation types. In this paper, we present theoretical and computational methods for obtaining the tensor from fully three dimensional PFC configurations. We derive an analytical expression for the defect line velocity in terms of continuous field variables, which is based on conservation of topological charge. The resulting dislocation motion is overdamped, and obeys the classical Peach-Koehler law. This result is used as a numerical tool to study the shrinkage of a dislocation loop in a PFC bcc lattice.

Another challenge for the PFC formalism under its classical dynamics is that it does not consider the relaxation of elastic excitations. Their characteristic relaxation time,  $\tau_E$ , is the faster time scale compared with the slow, dissipative relaxation time scale  $\tau_D$  of the phase field (which determines the dislocation motion). A first attempt at extending the model to include fast elastic relaxation considered a phenomenological second order

temporal derivative in the equation of motion for the phase field [22], which allowed for fast relaxation of short-wavelength elastic disturbances. Later efforts have included coupling the PFC phase field to a velocity field [23], various methods of coarse graining it to develop a consistent hydrodynamical description [24, 25], or coupling the PFC to an independent material distortion field [18]. Such approaches are necessary for a proper description of processes where elastic interactions are important, such as crack propagation and defect dynamics. Other efforts have been made to develop efficient modeling approaches in which the time scale of elastic interactions is *a priori* set to zero  $\tau_E = 0$ , i.e. when mechanical equilibrium is obeyed at all times. The latter approach is justified when studying plasticity phenomena where irreversible deformations are slow, including many of the applications mentioned such as creep and boundary driven grain motion. This approach was first introduced in Ref. [26] which involved relaxing elastic excitations separately and instantaneously within the amplitude equation formulation of the PFC model [27]. The same strategy was later developed for the PFC model in two dimensional isotropic 2D lattices by adding to the phase-field a correction at each time step that ensured instantaneous mechanical equilibrium [28, 29]. In this paper, we present a generalization of this approach to anisotropic crystals in three dimensions (PFC-MEq). Since a distorted phase field configuration determines the corresponding configurational stresses [21, 30], the method yields regularized stress profiles for dislocation lines in three dimensions down to the defect core. In the case of a point defect, it was shown in Ref. [29] that the stress field at the core agrees with the predictions of the non-singular theory of Ref. [31], and with gradient elasticity models [32, 33], indicating that the results obtained here can serve as benchmarks for similar theories in three dimensions. The specific example of a dislocation loop in a body-cubic-centered (bcc) lattice is considered, and the far-field stresses given by the  $\psi$  field are shown to coincide with predictions from continuum elasticity.

The rest of the paper is structured as follows. In Sec. II, we propose a theoretical method, that is also numerically versatile, for accurately extracting topological defects from the periodic  $\psi$ -field. This allows us to define the dislocation density tensor in terms of the phase field (Eq. (11)), and obtain the dislocation line velocity (Eq. (17)) from the motion of its phase singularities. These are key results, which are applied in several examples in Sec. III. First, we use the PFC model to numerically study the shrinkage of a dislocation loop in a bcc lattice. Then, we show analytically that Eq. (17) captures the overdamped motion of dislocations driven by the Peach-Koehler force, and hence by the local stress. Finally, we introduce the PFC-MEq model, and compare the shrinkage of the dislocation loop under PFC and PFC-MEq dynamics. While the results are qualitatively similar for the case of a shear dislocation loop, the constraint of mechanical equilibrium causes the shrinkage to

happen much faster. We then confirm that the stress field derived from the  $\psi$  field in the PFC-MEq model agrees with continuum elasticity theory in the far field, with no adjustable parameters, when the dislocation density obtained from Eq. (11) is used as the source of stress.

## II. THE KINEMATICS OF A DISLOCATION LINE IN THREE DIMENSIONS

We consider a periodic phase field  $\psi$  of a given crystal symmetry. A reference crystalline lattice (in the absence of defects) is defined by a set of  $N$  primary reciprocal vectors  $\{\mathbf{q}^{(n)}\}_{n=1}^N$  which defines the lattice constant  $a_0 \sim 2\pi/|\mathbf{q}^{(n)}|$ . Slowly varying complex amplitude or envelope functions  $\eta_n(\mathbf{r})$  can be defined near the transition point, for example by using a multiple scale expansion, so that  $\psi \approx \bar{\psi} + \sum_{n=1}^N \eta_n(\mathbf{r}) e^{i\mathbf{q}^{(n)} \cdot \mathbf{r}}$ . For our present purposes, we define here the amplitudes through demodulation of  $\psi$  as

$$\eta_n(\mathbf{r}) = e^{-i\mathbf{q}^{(n)} \cdot \mathbf{r}} \mathcal{F}^{-1} \left\{ e^{-\frac{a_0^2 (\mathbf{k} - \mathbf{q}^{(n)})^2}{2}} \mathcal{F}\{\psi\} \right\}, \quad (1)$$

where  $\mathcal{F}\{\psi\}$  denotes the Fourier transform of  $\psi$  ( $\mathcal{F}^{-1}$  is the inverse transform). A defect free lattice yields slowly varying amplitudes, whereas defects correspond to amplitudes  $\eta_n$  that have discontinuous phases  $\theta_n = \text{Arg}(\eta_n)$ , and hence vanishing magnitudes at defect cores. For a perfect lattice,  $\theta_n^{(0)} = 0$  and displacing a lattice plane by a slowly varying  $\mathbf{u}$  transforms the phase as  $\theta_n \rightarrow \theta_n^{(0)} - \mathbf{q}^{(n)} \cdot \mathbf{u}$ . Thus, the phase provides a direct measure of the displacement field  $\mathbf{u}(\mathbf{r})$  relative to the reference lattice, i.e.

$$\theta_n(\mathbf{r}) = -\mathbf{q}^{(n)} \cdot \mathbf{u}(\mathbf{r}) = -q_i^{(n)} u_i(\mathbf{r}), \quad (2)$$

where  $q_i^{(n)}$  denotes the  $i$ -th Cartesian coordinate of  $\mathbf{q}^{(n)}$ . It is possible to invert Eq. (2), and solve for the displacement field  $\mathbf{u}$  as function of the phases  $\theta_n$  and reciprocal vectors. We use the following identity which is valid for lattices with cubic symmetry, where all primary reciprocal lattice vectors have the same length  $q_0$  (see Appendix A)

$$\sum_{n=1}^N q_i^{(n)} q_j^{(n)} = \frac{N}{3} q_0^2 \delta_{ij}, \quad (3)$$

so that the displacement  $\mathbf{u}$  is given by,

$$\mathbf{u}(\mathbf{r}) = \frac{3}{N q_0^2} \sum_{n=1}^N \mathbf{q}^{(n)} \theta_n(\mathbf{r}). \quad (4)$$

An alternative view when a subset of the amplitudes is available instead, as e.g., from experimental imaging, is reported in Ref. [34]. The presence of crystal defects produces discontinuous displacement fields, which are captured by discontinuous phases in the complex amplitudes.

In fact, Eq. (4) shows that the discontinuity of the phase  $\theta_n$  is directly related to the discontinuity of  $\mathbf{u}$ , as shown in Fig. 1.

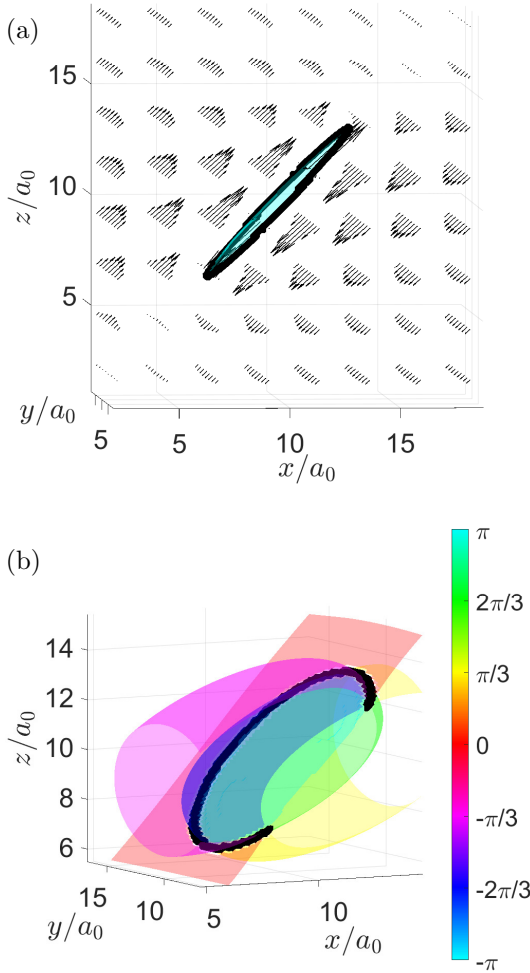


FIG. 1. (a) Example of a discontinuous displacement field  $\mathbf{u}$  in the presence of a dislocation loop (black line) with Burgers vector  $\mathbf{b}$  (Eq. (5)). (b) Isosurfaces of one of the phases  $\theta_n$  possessing the same discontinuity as the displacement field (Eq. (2)).

Consider now a general three dimensional crystal lattice that contains a dislocation line  $\mathcal{C}$ . For a point  $\mathbf{r}'$  on the dislocation line, we denote by  $\mathbf{t}'$  the tangent vector to  $\mathcal{C}$ . In addition, we introduce a local Cartesian plane  $\mathcal{N}'$  normal to  $\mathbf{t}'$ , such that the distance of an arbitrary point  $\mathbf{r}$  to a point  $\mathbf{r}'$  on  $\mathcal{C}$  is decomposed into an in-plane vector  $\Delta\mathbf{r}_\perp \perp \mathbf{t}'$  and a vector  $\Delta\mathbf{r}_\parallel \parallel \mathbf{t}'$ , i.e.  $\mathbf{r} - \mathbf{r}' = \Delta\mathbf{r}_\perp + \Delta\mathbf{r}_\parallel$ , see Fig. 2. The discontinuity across the surface spanned by the dislocation line  $\mathcal{C}$  defines the Burgers vector  $\mathbf{b}$  of the dislocation

$$\oint_{\Gamma'} d\mathbf{u} = \mathbf{u}^+ - \mathbf{u}^- = -\mathbf{b}, \quad (5)$$

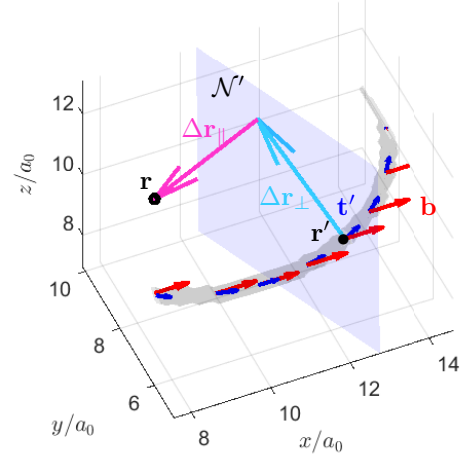


FIG. 2. The difference  $\mathbf{r} - \mathbf{r}'$  from a point  $\mathbf{r}$  to a point  $\mathbf{r}'$  on the line is decomposed into a 2D in-plane vector  $\Delta\mathbf{r}_\perp$ , which is the projection of  $\mathbf{r} - \mathbf{r}'$  onto the plane  $\mathcal{N}'$  normal to  $\mathbf{t}'$  and a distance  $|\Delta\mathbf{r}_\parallel|$  from this plane. In this figure,  $\Delta\mathbf{r}_\parallel \cdot \mathbf{t}' = -3.47a_0$  and  $|\Delta\mathbf{r}_\perp| = 3.42a_0$ .

where  $\mathbf{u}^+$  and  $\mathbf{u}^-$  are the values of the displacement field at each side of the branch cut, respectively. We use the negative sign convention relating the contour integral with the Burgers vector. Here,  $\Gamma'$  is a small circuit enclosing the dislocation line in the  $\mathcal{N}'$ -plane, directed according to the right-hand rule with respect to  $\mathbf{t}'$ . By using Eq. (2) and the fact that the Burgers vector  $\mathbf{b}$  is constant along the dislocation loop, we relate the Burgers vector to the phase  $\theta_n$  as

$$\oint_{\Gamma'} d\theta_n = - \oint_{\Gamma'} \mathbf{q}^{(n)} \cdot d\mathbf{u} = \mathbf{q}^{(n)} \cdot \mathbf{b} \equiv 2\pi s_n, \quad (6)$$

where  $s_n$  is the winding number of the phase  $\theta_n$  around the dislocation line. The dislocation density tensor associated with the line is [35]

$$\alpha_{ij}(\mathbf{r}) = b_j \delta_i^{(2)}(\mathcal{C}) = b_j \oint_{\mathcal{C}} dl'_i \delta^{(3)}(\mathbf{r} - \mathbf{r}'), \quad (7)$$

where  $b_j$  is the  $j$  component of the Burgers vector of the line, and  $dl'_i = t'_i dl'$  is the line element in the direction of the line.  $\delta_i^{(2)}(\mathcal{C})$  is a short-hand notation for the delta function, with dimension of inverse area, locating the position of the dislocation line for each component  $i$  of the dislocation density tensor. It is defined by the line integral over the dislocation line of the full delta function (which scales as inverse volume). The line density  $\rho_i^{(n)}(\mathbf{r})$  of topological defects in the amplitude  $\eta_n$  is obtained by contracting the dislocation density with  $\mathbf{q}^{(n)}$ , namely

$$\frac{1}{2\pi} q_k^{(n)} \alpha_{ik}(\mathbf{r}) = s_n \delta_i^{(2)}(\mathcal{C}) \equiv \rho_i^{(n)}(\mathbf{r}). \quad (8)$$

The defect is located at the position where the magnitude of the complex amplitude  $\eta_n$  goes to zero, which

coincides with phase singularities, as seen from Eq. (8) (also illustrated in Fig. 1 (b)). By a coordinate transformation of the delta function in Eq. (8), the line density can be represented in terms of the zeros of  $\eta_n$  as [36, 37]

$$\rho_i^{(n)} = \delta^{(2)}(\eta_n) D_i^{(n)}(\mathbf{r}), \quad (9)$$

where the vector field  $D_i^{(n)}(\mathbf{r})$  is given by

$$D_i^{(n)}(\mathbf{r}) = \frac{1}{2i} (\nabla \eta_n^* \times \nabla \eta_n)_i = \frac{1}{2i} \epsilon_{ijk} (\partial_j \eta_n^*) (\partial_k \eta_n), \quad (10)$$

and is directed along the tangent to the line. Each amplitude  $\eta_n$  with a singular phase  $\theta_n$  can be thought of as a vortex line at  $\eta_n = 0$ , such that we can reconstruct the dislocation density tensor from an appropriate summation over the modes with singular phases. In fact, the dislocation density tensor  $\alpha_{ij}$  is obtained by multiplying Eq. (8) by  $q_j^{(n)}$ , summing over the reciprocal modes and using Eq. (3) to arrive at

$$\alpha_{ij}(\mathbf{r}) = \frac{6\pi}{Nq_0^2} \sum_{n=1}^N q_j^{(n)} D_i^{(n)}(\mathbf{r}) \delta^{(2)}(\eta_n). \quad (11)$$

Further, the vector field  $D_i^{(n)}$  satisfies a conservation law which can be obtained by differentiating Eq. (10) with respect to time [36, 37]. We find  $\partial_t D_i^{(n)} + \epsilon_{ikl} \partial_k J_l^{(n)} = 0$ , with the associated current given by  $J_l^{(n)} = \Im(\partial_t \eta_n \partial_l \eta_n^*)$ . This relationship implies a topological conservation law for  $\alpha_{ij}$ ,  $\partial_t \alpha_{ij} + \epsilon_{ikl} \partial_k \mathcal{J}_{lj} = 0$ , with an associated tensor current  $\mathcal{J}_{lj}$  that follows from Eq. (11) after differentiating through the delta functions as

$$\mathcal{J}_{lj}(\mathbf{r}) = \frac{6\pi}{Nq_0^2} \sum_{n=1}^N q_j^{(n)} J_l^{(n)}(\mathbf{r}) \delta^{(2)}(\eta_n). \quad (12)$$

In analogy with plasticity theory [19], we assume that this general dislocation density current can be associated with the local velocity of the line  $\mathbf{v}$  through  $\mathcal{J}_{lj}^{(\alpha)} = \epsilon_{lmn} \alpha_{mj} v_n$ . Note that  $\mathcal{J}_{lj}^{(\alpha)}$  explicitly depends on  $\partial_t \eta_n$ , and hence on the law governing the temporal evolution of the phase field. By equating the two expressions in the vicinity  $R' = \{\mathbf{r}, |\mathbf{r} - \mathbf{r}'| \ll 1\}$  of a point  $\mathbf{r}'$  on the dislocation line, we can derive an explicit expression for the dislocation velocity  $v'_n$  at  $\mathbf{r}'$  in terms of the field variables  $\mathbf{D}^{(n)}(\mathbf{r}')$  and  $\mathbf{J}^{(n)}(\mathbf{r}')$ . For  $\mathbf{r} \in R'$ , we can write [19]

$$\mathbf{r} \in R' : \alpha_{ij} = t'_i b_j \delta^{(2)}(\Delta \mathbf{r}_\perp). \quad (13)$$

Thus, using that  $\mathcal{J}_{lj}(\mathbf{r}) \equiv \mathcal{J}_{lj}^{(\alpha)}(\mathbf{r})$ , we find

$$\begin{aligned} \mathbf{r} \in R' : \frac{6\pi}{Nq_0^2} \sum_{n=1}^N q_j^{(n)} J_l^{(n)} \delta^{(2)}(\eta_n) \\ = \epsilon_{lmn} t'_m b_j v'_n \delta^{(2)}(\Delta \mathbf{r}_\perp). \end{aligned} \quad (14)$$

In the vicinity of the defect line, we have that  $\delta_i^{(2)}(\mathcal{C}) = t'_i \delta^{(2)}(\Delta \mathbf{r}_\perp)$ , such that the transformation of the  $\delta$ -function from Eq. (8) and Eq. (9) imply that

$$\mathbf{r} \in R' : \delta^{(2)}(\eta_n) = s_n \frac{t'_i D_i^{(n)}}{|\mathbf{D}^{(n)}|^2} \delta^{(2)}(\Delta \mathbf{r}_\perp). \quad (15)$$

Inserting this into Eq. (14), contracting with  $b_j$ , and integrating over  $\Delta \mathbf{r}_\perp$ , we find

$$\mathbf{r} = \mathbf{r}' : \frac{12\pi^2}{Nq_0^2 |\mathbf{b}|^2} \sum_{n=1}^N s_n^2 \frac{t'_i D_i^{(n)}}{|\mathbf{D}^{(n)}|^2} J_l^{(n)} = \epsilon_{lmn} t'_m v'_n. \quad (16)$$

Since  $\mathbf{t}' \perp \mathbf{v}'$ , we can easily invert this relation to find  $\mathbf{v}'$ , and using that  $\mathbf{D}^{(n)} \parallel \mathbf{t}'$  gives

$$\mathbf{r} = \mathbf{r}' : v'_s = \frac{12\pi^2}{Nq_0^2 |\mathbf{b}|^2} \sum_{n=1}^N s_n^2 \frac{\epsilon_{slr} J_l^{(n)} D_r^{(n)}}{|\mathbf{D}^{(n)}|^2}. \quad (17)$$

Eqs. (11) and (17) are the key results of this paper. Eq. (11) defines the dislocation density tensor from the demodulated amplitudes  $\eta_n$  of the phase field, while Eq. (17) gives an explicit expression for the dislocation line velocity. Both equations bridge the continuum description based on the dislocation density and line velocity with the microscopic scale of the phase field.

### III. DISLOCATION MOTION IN A BCC LATTICE

We apply here the framework developed in Sec. II to a phase field crystal model of dislocation motion in a bcc lattice [1, 2, 38]. The free energy  $F_\psi$  is a functional of the phase field  $\psi$  over the domain  $\Omega$  given by

$$F_\psi = \int_\Omega \left[ \frac{\Delta B_0}{2} \psi^2 + \frac{B_0^x}{2} \psi \mathcal{L}^2 \psi - \frac{T}{3} \psi^3 + \frac{V}{4} \psi^4 \right] d\mathbf{r}, \quad (18)$$

where  $\mathcal{L} = q_0^2 + \nabla^2$ , and  $\Delta B_0$ ,  $B_0^x$ ,  $V$ , and  $T$  are constant parameters [13]. The dissipative relaxation of  $\psi$  reads as

$$\frac{\partial \psi}{\partial t} = \Gamma \nabla^2 \frac{\delta F_\psi}{\delta \psi}. \quad (19)$$

with constant mobility  $\Gamma$ . We will refer to Eq. (19) as the "classical" PFC dynamics. As a characteristic unit of time given these model parameters, we use  $\tau = (\Gamma B_0^x q_0^6)^{-1}$ . For appropriate parameter values, the ground state of this energy is a bcc lattice which is well described in the one mode approximation

$$\psi(\mathbf{r}) = \psi_0 + \sum_{n=1}^{12} \eta_n e^{i\mathbf{q}^{(n)} \cdot \mathbf{r}}, \quad (20)$$

where  $\psi_0$  is the average density and  $\{\mathbf{q}_n\}$  are the  $N = 12$  shortest reciprocal lattice vectors

$$\begin{aligned} \mathbf{q}^{(1)} &= q_0(0, 1, 1)/\sqrt{2}, & \mathbf{q}^{(4)} &= q_0(0, -1, 1)/\sqrt{2} \\ \mathbf{q}^{(2)} &= q_0(1, 0, 1)/\sqrt{2}, & \mathbf{q}^{(5)} &= q_0(-1, 0, 1)/\sqrt{2} \\ \mathbf{q}^{(3)} &= q_0(1, 1, 0)/\sqrt{2}, & \mathbf{q}^{(6)} &= q_0(-1, 1, 0)/\sqrt{2} \end{aligned} \quad (21)$$

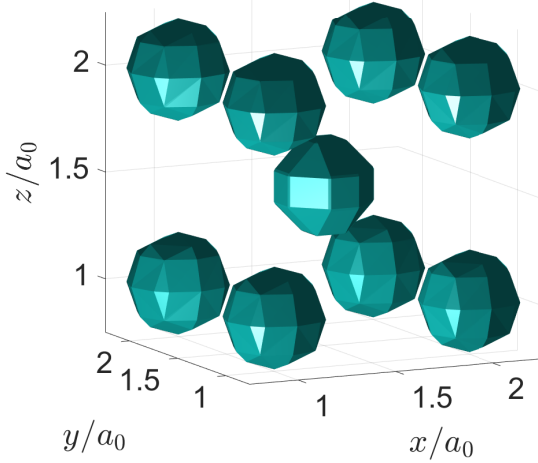


FIG. 3. A bcc unit cell in the PFC model shown by isosurfaces of constant  $\psi$ . Using the model parameters given in Sec. V,  $\psi(\mathbf{r})$  varies between peaks of  $\psi = 0.7447$  and troughs of  $\psi = -0.6148$  with the isosurfaces drawn at  $\psi = 0.0694$ .

with  $\mathbf{q}^{(n)} = -\mathbf{q}^{(n-6)}$  for  $n = 7, \dots, 12$ . Figure 3 shows one bcc unit cell of a phase-field initialized in the one-mode approximation. Given the equilibrium configuration, the lattice constant  $a_0$  will be used as the characteristic unit of length and the shear modulus  $\mu$  calculated from the phase-field will serve as the characteristic unit of stress [30]. As we see, the functional form of the free energy determines the base vectors  $\mathbf{q}^{(n)}$ , and no further assumptions about slip systems or constitutive laws for dislocation velocity (or plastic strain rates) need to be introduced.

The model parameters ( $\Delta B_0, B_0^x, T, V$ , and  $\Gamma$ ) and variables ( $F_\psi, \psi, \mathbf{r}$ , and  $t$ ) can be rescaled to a dimensionless form in which  $B_0^x = V = q_0 = \Gamma = 1$ , thus leaving only three tunable model parameters: the quenching depth  $\Delta B_0$ ,  $T$  and the average density  $\psi_0$  (due to the conserved nature of Eq. (19)). We employ these dimensionless units in the simulations, see Sec. VB.

#### A. Numerical analysis: shrinkage of a dislocation loop

In order to have a lattice containing one dislocation loop as initial condition in the PFC, we consider first the demodulation of the  $\psi$  field in the one mode approximation, and minimize the free energy (18) with respect to  $\eta_n$  to find the equilibrium amplitude  $\eta_0$  of a perfect, undistorted crystal. A dislocation loop is introduced into the perfect lattice by multiplying the equilibrium amplitudes by complex phases with the appropriate charges  $s_n$  (see Sec. VC) and then reconstructing the phase field  $\psi$

through Eq. (20). We then integrate Eq. (19) forward in time as detailed in Sec. VB. A fast relaxation follows from the initial configuration with the loop. This relaxation leads to the regularization of the singularity at the dislocation line ( $\eta_n \rightarrow 0$  for  $s_n \neq 0$ ) as achieved in PFC approaches [21, 29, 34]. From then onward,  $\psi$  evolves in time leading to the motion of the dislocation line which may be analyzed by the methods outlined in Sec. II.

Numerically, we approximate the  $\delta$  function in Eq. (11) as a sharply peaked 2D Gaussian distribution, i.e.,  $\delta^{(2)}(\eta_n) \simeq \exp(-\frac{|\eta_n|^2}{2\omega^2})/(2\pi\omega^2)$  with a standard deviation of  $\omega = \eta_0/10$ . Near the dislocation line, the dislocation density  $\alpha_{ij}$  thus takes the form of a sharply peaked function (Eq. (13)). The decomposition of  $\alpha_{ij}$  into its outer product factors  $t'_i$  and a Burgers vector density  $B_j = b_j\delta^{(2)}(\Delta\mathbf{r}_\perp)$  is done by singular value decomposition (see Sec. VA), and the Burgers vector of the point is extracted by performing a local surface integral in  $\mathcal{N}'$ . We prepare a  $35 \times 35 \times 35$  unit cell 3D PFC lattice on periodic boundary conditions with a resolution of  $\Delta x = \Delta y = \Delta z = a_0/7$ . A dislocation loop is introduced as the initial condition in the slip system given by a plane normal  $[-1, 0, 1]$  with slip direction (Burgers vector)  $\frac{a_0}{2}[1, -1, 1]$ . Figure 4(a) shows the initial dislocation density decomposed as described, where we also have calculated the velocity  $\mathbf{v}'$  at each point given by Eq (17).

In order to obtain the velocity of the dislocation loop segments, we identify  $M$  nodes on the loop and evaluate Eq. (17) by using numerical differentiation of the  $\psi$  field to calculate the amplitude currents  $J_l^{(n)}$ . To serve as a benchmark, we also calculate the circumference  $l_C$  of the dislocation loop  $\mathcal{C}$  at each time (further details in Sec. VD), so that we compare the rate of shrinkage  $|\partial_t R|$

$$|\partial_t R| = \frac{1}{2\pi} |\partial_t l_C|, \quad (22)$$

(solid blue line in Fig. 4(b)) to the average velocity of the  $M$  dislocation nodes

$$\bar{v} = \frac{1}{M} \sum_{m=1}^M |\mathbf{v}^{(m)}|, \quad (23)$$

(dashed blue line in Fig. 4(b)) where  $\mathbf{v}^{(m)}$  is the velocity of dislocation at node  $m$ , calculated by the velocity formula Eq. (17).  $|\partial_t R|$  and  $\bar{v}$  should agree in the case of the shrinking of a perfectly circular loop and the figure shows excellent agreement between the two. Interestingly, we observe that both are sensitive to the Peierls like barriers during their motion, as shown by the oscillations in Fig. 4(b)). The maxima are separated by  $2\pi a_0$ , confirming that the oscillation is related to the motion of a loop segment over one lattice spacing  $a_0$  [39]. This observation confirms that even though Eqs. (11) and (17) are continuum level descriptions of the system, they still exhibit behavior related to the underlying lattice configuration. The initial fast drop in velocity is due to the fast

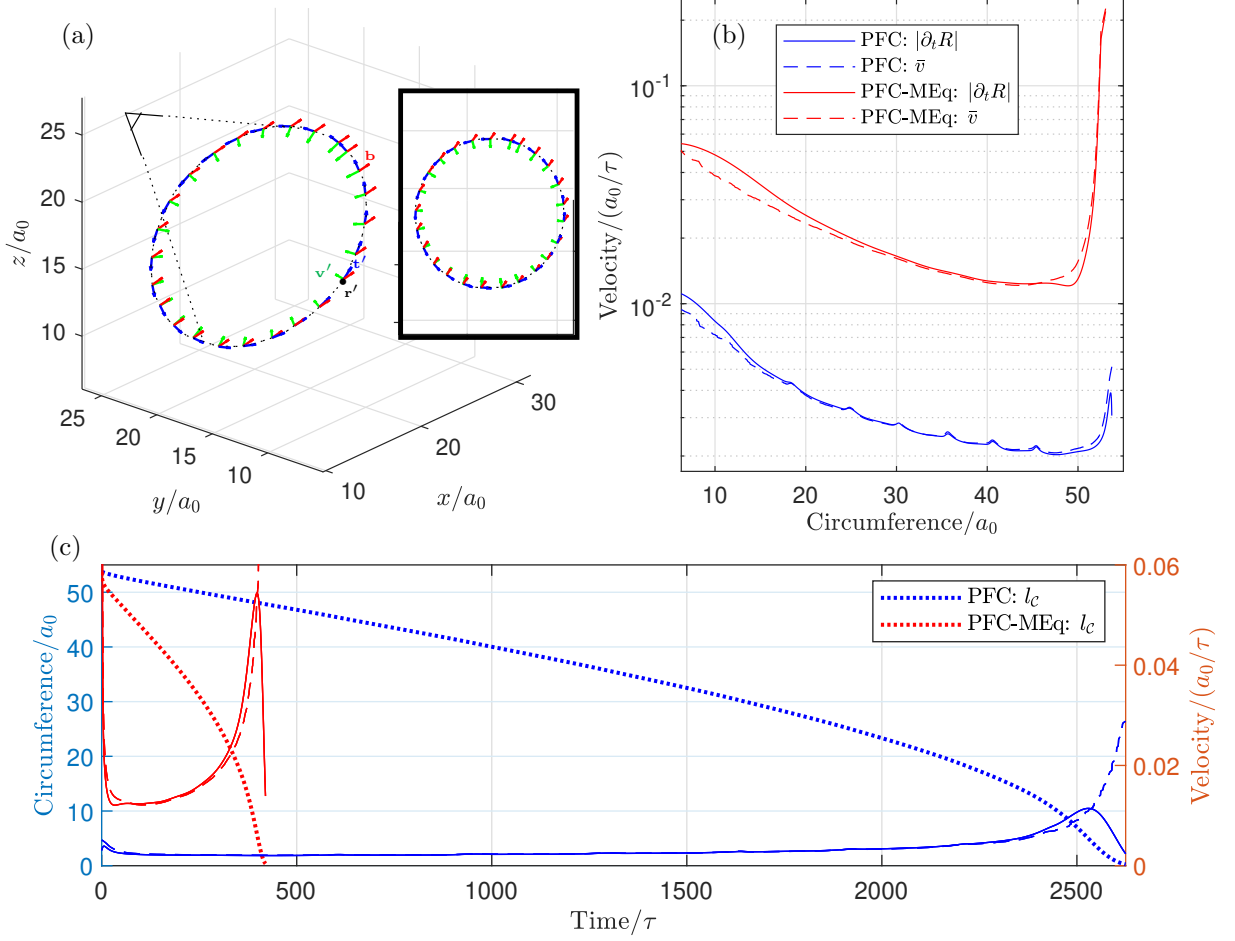


FIG. 4. (a) The initial dislocation loop in a  $35 \times 35 \times 35$  bcc PFC lattice with periodic boundary conditions. The dislocation loop is on the slip system given by plane normal  $[-1, 0, 1]$  and slip direction (Burgers vector)  $\frac{a_0}{2}[1, -1, 1]$ . Inset: the dislocation loop viewed from the indicated angle. (b) Comparison of average point velocity  $\bar{v}$  (Eq. (23)) to the average loop radius shrinkage velocity  $|\partial_t R|$  (Eq. (22)) as functions of the loop circumference. PFC and PFC-MEq refer, respectively, to the classical PFC model, and the PFC model constrained to mechanical equilibrium as introduced in Sec. III C. (c) The circumference  $l_c$  of the dislocation loop. Superimposed on the right y-axis are the velocities of panel (b) as functions of time.

relaxation of the initial condition. The evolution of the variables under the dynamics of Eq. (19) are shown together with the evolution given by the PFC-MEq model which will be introduced in Sec. III C.

### B. Theoretical analysis: Peach Koehler force

In this section, we show that the general expression Eq. (17) of the defect velocity agrees with the dissipative motion of a dislocation as given by the classical Peach-Koehler force [19]. To calculate an analytical expression for the amplitude currents  $J_i$ , we employ the amplitude formulation of the PFC model, which directly expresses the free energy and dynamical equations in terms of the complex amplitudes  $\eta_n$  [27, 40]. For our lattice symmetry, real valuedness of  $\psi$  requires that  $\eta_{n+6} = \eta_n^*$ , and the

dynamical equations need only consider the amplitudes  $\{\eta_n\}_{n=1}^6$ . By substituting Eq. (20) in  $F_\psi$  and integrating over the unit cell, under the assumption of slowly-varying amplitudes, one obtains the following free energy as a function of the complex amplitudes,

$$F_\eta = \int_\Omega \left[ \frac{\Delta B_0}{2} \Phi + \frac{3v}{4} \Phi^2 + \sum_{n=1}^6 \left( B_0^x |\mathcal{G}_n \eta_n|^2 - \frac{3v}{2} |\eta_n|^4 \right) + f^s(\{\eta_n\}, \{\eta_n^*\}) \right] d\mathbf{r}, \quad (24)$$

where  $\mathcal{G}_n = \nabla^2 + 2i\mathbf{q}_n \cdot \nabla$  and  $\Phi = 2 \sum_{n=1}^6 |\eta_n|^2$ .  $f^s(\{\eta_n\}, \{\eta_n^*\})$  is a polynomial in  $\eta_n$  and  $\eta_n^*$  that depends in general on the specific crystalline symmetry under consideration [12, 27, 41] (here bcc, see Appendix B for its expression). Equation (24) is obtained when considering

a set of vectors  $\mathbf{q}$  of length  $q_0$ , while similar forms may be achieved when considering different length scales [12, 42]. The evolution of  $\eta_n$ , which follows from from Eq. (19) is [12, 27],

$$\frac{\partial \eta_n}{\partial t} = -\Gamma q_0^2 \frac{\delta F}{\delta \eta_n^*}, \quad (25)$$

with

$$\frac{\delta F}{\delta \eta_n^*} = [\Delta B_0 + B_0^x \mathcal{G}_n^2 + 3v(\Phi - |\eta_n|^2)] \eta_n + \frac{\partial f^s}{\partial \eta_n^*}. \quad (26)$$

Near a defect core (where a few of the amplitudes vanish), it can be shown that the equations for the amplitudes decouple (see Appendix B), such that their evolution near the core is

$$\partial_t \eta_n \approx -\Gamma B_0^x q_0^2 \mathcal{G}_n^2 \eta_n. \quad (27)$$

Therefore the complex amplitudes of a stationary dislocation satisfy  $\mathcal{G}_n^2 \eta_n^{(0)} = 0$ . We now add an externally imposed, continuous displacement  $\tilde{\mathbf{u}}$  [21].  $\tilde{\mathbf{u}}$  might represent the far-field displacement arising from a different dislocation line segment, or associated with an externally imposed stress. This displacement is in addition to the discontinuous displacement field  $\mathbf{u}$ , described in Sec. II, which is captured in the stationary solution  $\eta_n^{(0)}$ , and defines the Burgers vector of the dislocation line (Fig. 1). For small distortions,  $|\nabla \tilde{\mathbf{u}}| \ll 1$ , the added distortion leads to  $\eta_n = \eta_n^{(0)} e^{-i\mathbf{q}_n \cdot \tilde{\mathbf{u}}}$ . Inserting this into Eq. (27), we find

$$D_i^{(n)} = \frac{1}{2i} \epsilon_{irs} (\partial_r \eta_n^{(0)*}) (\partial_s \eta_n^{(0)}), \quad (28)$$

which only depends on  $\eta_n^{(0)}$ . The corresponding defect density current is

$$J_l^{(n)} = 4\Gamma B_0^x q_0^2 q_i^{(n)} (\partial_k \tilde{u}_i) \Im \left( i(\partial_l \eta_n^{(0)*}) (\partial_k + i q_k^{(n)}) \mathcal{G}_n \eta_n^{(0)} \right). \quad (29)$$

Arguably, the simplest solution of Eq. (27) is the isotropic, simple vortex where  $\eta_n^{(0)}$  is linear with the distance from the core and  $s_n = \pm 1$ . We assume that on very short distances, the defect line is straight, such that the solution is  $\eta_n^{(0)} \propto x_\perp + i s_n y_\perp$ , by using the position vector decomposition from Sec. II,  $\mathbf{r} - \mathbf{r}' = \Delta \mathbf{r}_\perp + \Delta \mathbf{r}_\parallel$  with  $\mathbf{r}' = 0$ . The gradients of  $\eta_n^{(0)}$  can be evaluated in these coordinates relative to the line, and the resulting defect current is

$$J_l^{(n)} = -8\Gamma B_0^x q_0^2 q_i^{(n)} q_k^{(n)} q_m^{(n)} (\partial_k \tilde{u}_i) \Im \left( i(\partial_l \eta_n^{(0)*}) (\partial_m \eta_n^{(0)}) \right). \quad (30)$$

In terms of the local tangent vector  $\mathbf{t}'$ , we get  $D_i^{(n)} \propto s_n t'_i$ , and  $\Im \left( i(\partial_l \eta_n^{(0)*}) (\partial_m \eta_n^{(0)}) \right) \propto \delta_{lm} - t'_l t'_m$ , which

leads to a dislocation velocity given by

$$v'_s = -\epsilon_{slr} \frac{\Gamma \pi}{|\mathbf{b}|^2} b_j t'_r 4B_0^x \sum_{n=1}^{12} q_i^{(n)} q_j^{(n)} q_k^{(n)} q_l^{(n)} (\partial_k \tilde{u}_i) = \frac{\Gamma \pi}{\eta_0^2 |\mathbf{b}|^2} \epsilon_{srl} t'_r \tilde{\sigma}_{lj} b_j, \quad (31)$$

where  $\tilde{\sigma}_{lj}$  is the stress tensor for a bcc PFC that has been deformed by  $\tilde{\mathbf{u}}$ , [30]

$$\tilde{\sigma}_{lj}(\mathbf{r}) = 4B_0^x \eta_0^2 \sum_{n=1}^{12} q_i^{(n)} q_j^{(n)} q_k^{(n)} q_l^{(n)} \partial_k \tilde{u}_i. \quad (32)$$

Thus, the velocity of the dislocation line is proportional to the stress on the line. In vectorial form, this equation reads

$$\mathbf{v} = M \mathbf{t} \times (\tilde{\boldsymbol{\sigma}} \cdot \mathbf{b}). \quad (33)$$

with isotropic mobility  $M = \frac{\Gamma \pi}{|\mathbf{b}|^2 \eta_0^2}$ .

Note that a stationary dislocation induces a stress field  $\sigma_{ij}^{(0)}$ , but only the imposed stress  $\tilde{\sigma}_{ij}$  appears in the equation above. This is analogous to how the stress field of the dislocation itself is not included when the Peach-Koehler force as calculated in continuum plasticity theory [19]. Thus, if  $\sigma_{ij}^\psi$  is the configurational stress of the phase field at any given time, the part responsible for the motion of the dislocation motion is the imposed stress

$$\tilde{\sigma}_{ij} = \sigma_{ij}^\psi - \sigma_{ij}^{(0)}. \quad (34)$$

Note that the stationary solution necessarily satisfies mechanical equilibrium,  $\partial_j \sigma_{ij}^{(0)}$ , so that if the configurational PFC stress  $\sigma_{ij}^\psi$  is in mechanical equilibrium, so is the imposed stress  $\tilde{\sigma}_{ij}$  on the dislocation segment. The imposed stress used can be attributed to external load, other dislocations, or other parts of the dislocation loop.

As we see, this framework predicts a defect mobility which is isotropic. As such, it does not discriminate between dislocation climb and glide motion. Numerically however, we have seen that at deeper quenches  $\Delta B_0$ , climb motion is prohibited in the PFC model. The result in this section should therefore be interpreted as a first-order approximation, valid at shallow quenches. This apparent equal mobility for glide and climb may result from the employment of the amplitude phase-field model (which is only exact for  $|\Delta B_0| \rightarrow 0$ ) or the assumption of an isotropic defect core in the calculation.

### C. PFC dynamics constrained to mechanical equilibrium (PFC-MEq)

In the previous section, we found that the motion of a dislocation is governed by a configurational stress  $\sigma_{ij}^\psi$  which derives from the PFC free energy. Since this stress is a functional only of the phase field configuration, it

does not satisfy, in general, the condition of mechanical equilibrium. References [21, 30] give an explicit expression for this stress defined as the variation of the free energy with respect to distortion,

$$\sigma_{ij}^\psi = -2B_0^x \langle \mathcal{L}\psi \partial_{ij}\psi \rangle, \quad (35)$$

where  $\langle \cdot \rangle$  is a spatial average over  $1/q_0$  in order to eliminate the base periodicity of the undistorted phase field [30].

In this section, we discuss a modification of the PFC in three dimensions and in an anisotropic lattice so as to maintain elastic equilibrium in the medium while  $\psi$  evolves according to Eq. (19). Let  $\psi^{(U)}$  be the field that results from the evolution defined by Eq. (19) alone. At each time, we define

$$\psi(\mathbf{r}) = \psi^{(U)}(\mathbf{r} - \mathbf{u}^\delta), \quad (36)$$

where  $\mathbf{u}^\delta$  is a small compatible displacement computed so that the configurational stress associated with  $\psi(\mathbf{r})$  is divergence free. We now show a method to determine  $\mathbf{u}^\delta$ . Suppose that at some time  $t$  the PFC configuration  $\psi$  has an associated configurational stress  $\sigma_{ij}^{\psi,U}$  (from Eq. (35), where  $\partial_j \sigma_{ij}^{\psi,U} \neq 0$ ). Within linear elasticity, the stress  $\sigma_{ij}^\psi$  after displacement of the current configuration by  $\mathbf{u}^\delta$  is given by

$$\sigma_{ij}^\psi = \sigma_{ij}^{\psi,U} + C_{ijkl} e_{kl}^\delta \quad (37)$$

where  $C_{ijkl}$  is the elastic constant tensor, and  $e_{ij}^\delta = \frac{1}{2}(\partial_i u_j^\delta + \partial_j u_i^\delta)$ .  $\mathbf{u}^\delta$  is determined by requiring that

$$\partial_j \sigma_{ij}^\psi = \partial_j (\sigma_{ij}^{\psi,U} + C_{ijkl} e_{kl}^\delta) = 0. \quad (38)$$

By using the symmetry  $i \leftrightarrow j$  of the elastic constant tensor, we can rewrite this equation explicitly in terms of  $\mathbf{u}^\delta$ ,

$$g_i^{\psi,U} + C_{ijkl} \partial_{jk} u_l^\delta = 0, \quad (39)$$

where

$$g_i^\psi = \partial_j \sigma_{ij}^\psi = \left\langle \frac{\delta F_\psi}{\delta \psi} \partial_i \psi - \partial_i f \right\rangle \quad (40)$$

is the body force from the stress [30]. The quantity  $f$  is the free energy density from Eq. (18).

Given the periodic boundary conditions used, the system of equations (39) is solved by using a Fourier decomposition with the Green's function for elastic displacement in cubic anisotropic materials [43]. Once  $\mathbf{u}^\delta$  is obtained,  $\psi$  is updated according to Eq. (36), and evolved according to Eq. (19) from its current state  $\psi(t)$  to  $\psi^{(U)}(t + \Delta t)$ . In practice, we have found that numerically it is sufficient to impose this correction every few time steps. Note that Eqs. (39) can, in general, be solved for any elastic constant tensor, so that the method

introduced is not limited to cubic anisotropy. Possible limitations of the methodology are outlined in Sec. V.

Figure 4 contrasts numerical results for the evolution of an initial dislocation loop with and without using the method just described. The computed line velocities are very different as they are highly sensitive to the local stress experienced by the dislocation loop segments. This stems from the fact that under classical PFC dynamics, the stress is always given by  $\sigma_{ij}^{\psi,U}$ , and a consequence of the results from Sec. IIIB is that the velocity of an element of the defect line will be quite different depending on whether the stress acting on it is  $\sigma_{ij}^{\psi,U}$  or  $\sigma_{ij}^\psi$ . Figure 5 shows the dislocation loop after its circumference has shrunk to 90% of its initial value, and the resulting  $xz$  component of the stress for both models. As predicted, the correction provided by the PFC-MEq model is necessary to relax the stress originating from the initial loop. The figure shows a large residual stress far from the dislocation loop that can only decay diffusively in the standard phase field model. Indeed, we have verified numerically that the configurational stress is only divergenceless for the PFC-MEq model. We note that given the simple loop geometry chosen, its shape remains approximately circular for both models. The line speed, however, is quite different.

#### D. Comparison with continuum elasticity

Since Eq. (11) allows for the computation of the dislocation density tensor directly from the phase field, we show here the resulting elastic stress from standard continuum mechanics. The dislocation density  $\alpha_{ik}$  determines the incompatibility of the distortion,

$$\epsilon_{ilm} \partial_l u_{mk} = -\alpha_{ik}, \quad (41)$$

where  $u_{kl}$  is the distortion tensor, which away from defects can be written as  $u_{kl} = \partial_k u_l$ . In addition, the distortion  $u_{kl}$  satisfies the equilibrium condition

$$\partial_j C_{ijkl} u_{kl} = 0, \quad (42)$$

where  $C_{ijkl}$  is the tensor of elastic constants. Due to the symmetry of this tensor under  $k \leftrightarrow l$ , this equation only involves the strain, the symmetric part of  $u_{kl}$ . Equations (41) - (42) are nominally a set of 12 partial differential equations that determines 9 components of the distortion tensor  $u_{kl}$ . In Sec. VE, we show that the vanishing of the divergence of Eq. (41) reduces the number of independent equations to 9, and that the distortion  $u_{kl}$  can then be obtained from the dislocation density tensor by matrix inversion in Fourier space (given the periodic boundary conditions assumed on the medium). The stress field is then  $\sigma_{ij}^{(\alpha)} = C_{ijkl} u_{kl}$ .

Figure 6 shows all the stress components after the dislocation loop has shrunk to 90% of its initial diameter for both dynamical models, as well as the stress computed directly from the dislocation density tensor as a source



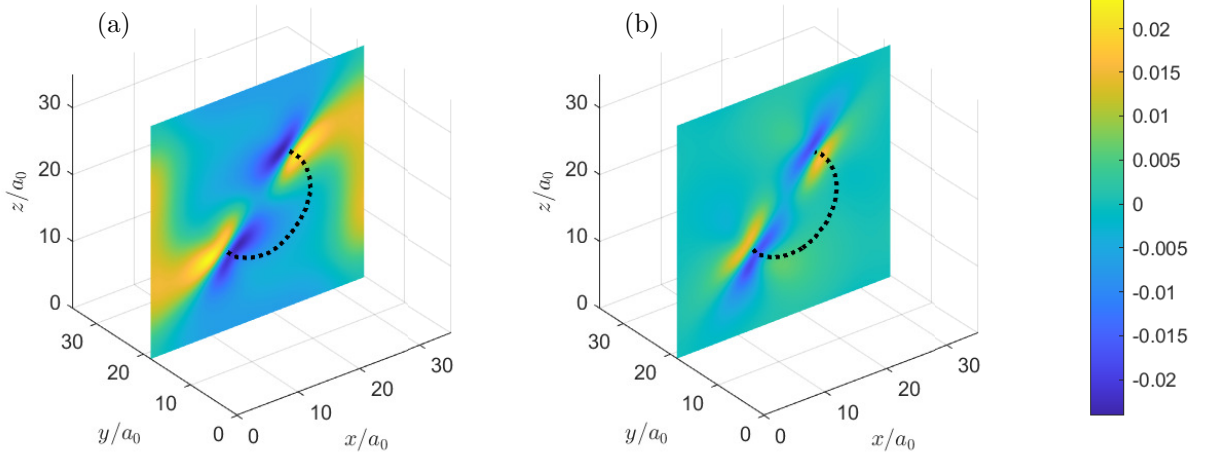


FIG. 5. In-plane sections ( $y = 17.5a_0$ ) of the configurational stress  $\sigma_{xz}^\psi/\mu$  for the dislocation loop after shrinking to 90% of its initial circumference under (a) PFC dynamics and (b) PFC-MEq dynamics. Because the latter evolves faster, the snapshots are taken at different times, namely  $t = 389.0\tau$  and  $t = 41.5\tau$ , respectively. A lot of residual (unrelaxed) stress is visible in the configurational stress for the classical PFC model.

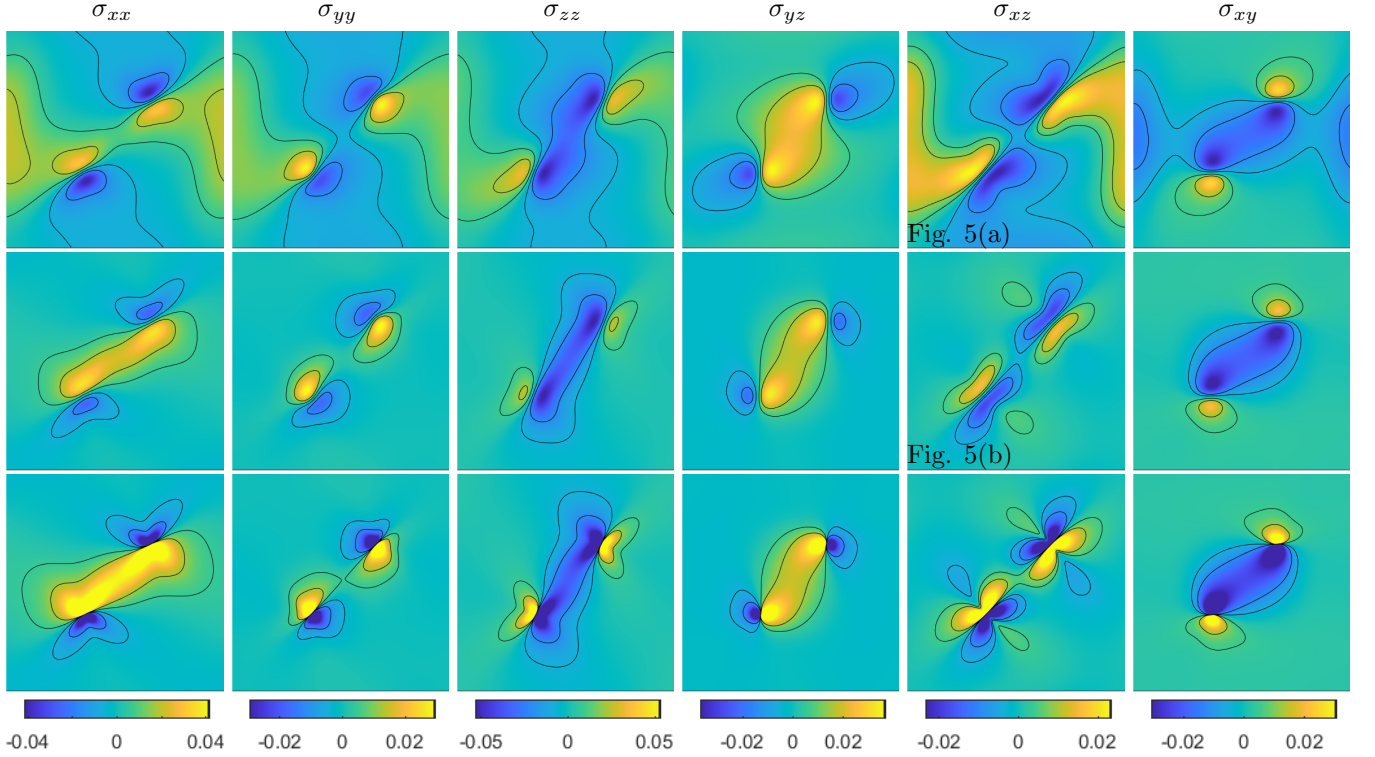


FIG. 6. In-plane sections ( $y = 17.5a_0$ ) of the stresses for the dislocation loop after it has shrunk to 90% of its initial circumference in (top row) the PFC model  $\sigma_{ij}^{\psi,U}$ , (middle row) the PFC-MEq model  $\sigma_{ij}^\psi$  and (bottom row) the prediction from continuum elasticity  $\sigma_{ij}^{(\alpha)}$  using the dislocation density extracted from the PFC as a source. The stresses predicted from continuum elasticity are singular, so the colorbar for each column is saturated at  $\pm \max(|\sigma_{ij}^{\psi,U}|)$  and contour lines are drawn at  $\pm 15\%$ ,  $\pm 40\%$  of this value. For the comparison, we have subtracted from  $\sigma_{ij}^{\psi,U}$  and  $\sigma_{ij}^\psi$  their mean values (see text). The stresses are given in units of the shear modulus  $\mu$ .

of distortion [44]. Note that the mean value of the components of  $\sigma_{ij}^{(\alpha)}$ , is not determined by Eqs. (41) - (42), and is set to zero. In this comparison, we have also subtracted from  $\sigma_{ij}^\psi$  its mean value. As expected, the stresses obtained from the PFC-MEq model agree well with  $\sigma_{ij}^{(\alpha)}$ . The small differences observed are due to the fact that  $\sigma_{ij}^{(\alpha)}$  derives from a singular dislocation density source (as produced by the  $\delta$ -functions in Eq. (11)), while the stress obtained from the phase field has a natural stress regularization at the defect core. Investigating exactly which length scale of core regularization derives from the PFC model is an open and interesting question that we will address in the future.

#### IV. CONCLUSIONS

We have introduced a theoretical method, and the associated numerical implementation, to study topological defect motion in a three dimensional, anisotropic, crystalline lattice. The dislocation density tensor and dislocation velocity are directly defined from a spatially periodic phase field, using general expressions identifying dislocations as bound vortex lines of the complex amplitudes of the phase field.

To illustrate the method, we have studied the motion of a shear dislocation loop, and found that it accurately tracks the loop position, circumference, and velocity. As an application of the framework, we have shown that under certain simplifying assumptions, overdamped dislocation velocity follows from a Peach-Koehler force, with the defect mobility determined by equilibrium properties of the lattice. We have introduced the PFC-MEq model for three dimensional anisotropic media which constrains the classical PFC model evolution to remain in mechanical equilibrium at all times, and shown that loop motion is much faster with this modification. The PFC-MEq model produces stress profiles that are in agreement, especially far from the defect core, to stress fields directly computed from the instantaneous dislocation density tensor.

In summary, we have presented a comprehensive framework, based on the phase field crystal model, for the analysis of plastic defect motion in crystalline solids. Starting from a free energy that has a ground state of the proper symmetry, the framework naturally leads to defect topology and kinematics laws, elastic stresses induced by defects, and a Peach-Koehler force, with an explicit expression for the line segment mobility.

#### V. METHODS

##### A. Dislocation density tensor decomposition

A singular value decomposition of  $\alpha$  is introduced as  $\alpha = U\Sigma V^T$ , where  $\Sigma$  is a diagonal matrix containing the singular values of  $\alpha$ , and  $U$  and  $V$  are unitary ma-

trices containing the normalized eigenvectors of  $(\alpha\alpha^T)$  and  $(\alpha^T\alpha)$ , respectively. We assume that the dislocation density tensor can be written as the outer product of the unitary tangent vector  $\mathbf{t}$  and a local spatial Burgers vector density  $\mathbf{B}(\mathbf{r})$ , i.e.,  $\alpha_{ij} = t_i B_j$ . Under this assumption, one finds  $\Sigma$  with only one non zero singular value,  $|\mathbf{B}|$ , and the columns of  $U$  and  $V$  that correspond to this singular value will be  $\mathbf{t}$  and  $\frac{\mathbf{B}}{|\mathbf{B}|}$ , respectively.

##### B. Evolution of the phase field

The temporal evolution of the phase field is governed by Eq. (19). The dimensionless parameters of the free energy were chosen as follows in order to yield a bcc ground state:  $\Delta B_0 = -0.3$ ,  $B_0^x = 1$ ,  $T = 0$  and  $V = 1$ . Lengths have been made dimensionless by choosing  $|\mathbf{q}^{(n)}| = q_0 = 1$ . The resulting lattice constant for the bcc structure is  $a_0 = 2\pi\sqrt{2}$ . Given the conserved dynamics of Eq. (19), the spatial average value  $\psi_0$  also becomes an input parameter which we have chosen to be  $\psi_0 = -0.325$ . The dimensionless model parameters give a dimensionless characteristic time scale  $\tau = 1$ .

In all cases the computational domain considered includes  $35 \times 35 \times 35$  base periods of the undistorted bcc lattice, with grid spacing  $\Delta x = \Delta y = \Delta z = a_0/7$ . Periodic boundary conditions are used throughout. Equation (19) is integrated forward in time with an explicit method [45], and  $\Delta t = 0.1$ . A Fourier decomposition of the spatial fields is introduced to compute the spatial derivatives of the fields, while nonlinear terms are computed in real space.

We implement the correction scheme of Eq. (36) every 5 iterations of the phase field evolution. We have chosen this update frequency so that the field  $\mathbf{u}^\delta$  remains small. If  $u_{\max} = \max_{\mathbf{r} \in \text{Domain}}(\mathbf{u}^\delta(\mathbf{r})) > 0.1a_0$ , we rescale  $\mathbf{u}^\delta$  so that  $u_{\max} = 0.1a_0$ , and repeat the process again until elastic equilibrium is achieved. Typically, when initializing the PFC field with a dislocation,  $\sim 5$  such iterations are needed, after which,  $u_{\max}$  is on the order of  $0.01a_0$ .

##### C. Initializing a dislocation loop in the PFC model

In this section, we show how to multiply the initial amplitudes  $\eta_0$  with complex phases, to produce a dislocation loop with Burgers vector  $\mathbf{b}$  in a slip plane given by normal vector  $\mathbf{n}$  (see Sec. III A). Given a point  $\mathbf{r}$ , it belongs to a plane  $\mathcal{N}'$  perpendicular to  $\mathbf{t}'$  for some point  $\mathbf{r}'$  on the dislocation loop (see Figure 7). This plane also intersects the diametrically opposed point  $\mathbf{r}''$  of the dislocation loop. If  $\mathbf{r}_0$  is the center of the loop, the distance vector  $\mathbf{r} - \mathbf{r}_0$  lies in  $\mathcal{N}'$ . Let  $(m_1, m_2)$  be the first and second coordinate in the Cartesian coordinate system defined by the right-handed orthonormal system  $\{(\mathbf{n} \times \mathbf{t}'), \mathbf{n}, \mathbf{t}'\}$  centered at  $\mathbf{r}_0$ . If  $m_1 > 0$ , we get from

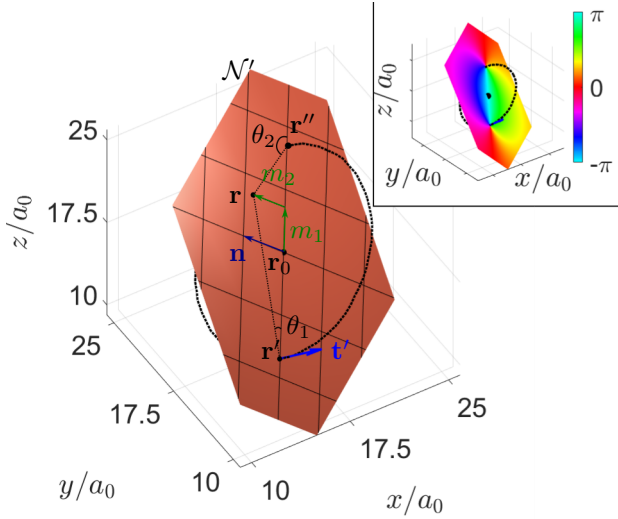


FIG. 7. Geometry of the circular dislocation loop in a slip plane given by the normal vector  $\mathbf{n}$ .  $\mathcal{N}'$  is the plane normal to the tangent vector  $\mathbf{t}'$  upon which we impose a Cartesian coordinate system to determine the angles  $\theta_1, \theta_2$  that are used to construct the (inset) initial amplitude phase configuration. For more details, see Section V C.

geometrical considerations

$$m_2 = (\mathbf{r} - \mathbf{r}_0) \cdot \mathbf{n} \quad (43)$$

$$m_1 = |(\mathbf{r} - \mathbf{r}_0) - m_2 \mathbf{n}|. \quad (44)$$

Both  $m_1$  and  $m_2$  are thus determined by  $\mathbf{r}$ ,  $\mathbf{r}_0$  and the normal vector to the loop plane  $\mathbf{n}$ .  $\theta_1$  ( $\theta_2$ ) is the angle between  $\mathbf{r} - \mathbf{r}'$  ( $\mathbf{r} - \mathbf{r}''$ ) and  $\mathbf{n} \times \mathbf{t}'$  in the plane  $\mathcal{N}'$  and are found numerically by using the four-quadrant inverse tangent  $\text{atan2}(y, x)$ , so that

$$\theta_1 = \text{atan2}(m_2, m_1 + R) \quad (45)$$

$$\theta_2 = \text{atan2}(m_2, m_1 - R), \quad (46)$$

where  $R$  is the radius of the loop. For each point  $\mathbf{r}$ , we determine  $\theta_1(\mathbf{r})$  and  $\theta_2(\mathbf{r})$  according to the equations above and initiate the PFC with the phases

$$\eta_n = \eta_0 e^{i s_n (\theta_1(\mathbf{r}) - \theta_2(\mathbf{r}))}, \quad (47)$$

where  $s_n = \frac{1}{2\pi} \mathbf{q}^{(n)} \cdot \mathbf{b}$  is given in Table I. This ensures that the complex phases have the right topological charge (Eq. (6)). The inset in Fig. 7 shows the phase of  $e^{i(\theta_1 - \theta_2)}$  in  $\mathcal{N}'$  for  $\mathbf{n} = \frac{1}{\sqrt{2}}[-1, 0, 1]$ , which is the slip plane chosen in the simulation in Sec. III A. Note that points  $\mathbf{r}$  for which  $m_1 < 0$  are computed by the same equation for the tangent vector at  $\mathbf{r}''$ , with the same formula, thus validating the Eqs. (45)–(46) for all values in  $\mathcal{N}'$ . Since the expressions are independent of the particular plane  $\mathcal{N}'$  and each point  $\mathbf{r}$  belongs to one such plane, they are also valid for all points in the simulation domain.

$\mathbf{b}$	$s_1$	$s_2$	$s_3$	$s_4$	$s_5$	$s_6$
$\frac{a_0}{2}(-1, 1, 1)$	1	0	0	0	1	1
$\frac{a_0}{2}(1, -1, 1)$	0	1	0	1	0	-1
$\frac{a_0}{2}(1, 1, -1)$	0	0	1	-1	-1	0
$\frac{a_0}{2}(1, 1, 1)$	1	1	1	0	0	0
$a_0(1, 0, 0)$	0	1	1	0	-1	-1
$a_0(0, 1, 0)$	1	0	1	-1	0	1
$a_0(0, 0, 1)$	1	1	0	1	1	0

TABLE I. Dislocation charges  $s_n = \frac{1}{2\pi} \mathbf{b} \cdot \mathbf{q}^{(n)}$  for different Burgers vectors  $\mathbf{b}$  in the bcc lattice.  $\mathbf{q}^{(n)}$  is defined in Eq. (21).

#### D. Calculating the perimeter of a dislocation loop

To calculate numerically the perimeter of a dislocation loop, recall that

$$\alpha_{ij} = b_j \oint_{\mathcal{C}} dl'_i \delta^{(3)}(\mathbf{r} - \mathbf{r}'_{(l)}), \quad (48)$$

where we have added a subscript ( $l$ ) onto  $\mathbf{r}'$  to emphasize that it is the point on the loop as indexed by the line element  $d\mathbf{l}$ . Taking the double dot product with itself, we find

$$\alpha_{ij} \alpha_{ij} = |\mathbf{b}|^2 \oint_{\mathcal{C}} \oint_{\mathcal{C}} dl'_i dm'_i \delta^{(3)}(\mathbf{r} - \mathbf{r}'_{(l)}) \delta^{(3)}(\mathbf{r} - \mathbf{r}'_{(m)}). \quad (49)$$

The contributions to this integral will only come from points on the loop  $\mathcal{C}$  and only when  $\mathbf{r}'_{(l)} = \mathbf{r}'_{(m)}$ , where  $dl'_i = dm'_i$ , so  $dl_i dm_i = (d\mathbf{l})^2 = |dl_i|^2 = |dl_i| |dm_i|$ . Thus

$$\begin{aligned} \alpha_{ij} \alpha_{ij} &= |\mathbf{b}|^2 \oint_{\mathcal{C}} |dl'_i| \delta^{(3)}(\mathbf{r} - \mathbf{r}'_{(l)}) \oint_{\mathcal{C}} |dm'_i| \delta^{(3)}(\mathbf{r} - \mathbf{r}'_{(m)}) \\ &= |\mathbf{b}|^2 \left( \oint_{\mathcal{C}} |dl'_i| \delta^{(3)}(\mathbf{r} - \mathbf{r}'_{(l)}) \right)^2. \end{aligned} \quad (50)$$

Taking the square root and integrating over all space, we find

$$\int d^3r \sqrt{\alpha_{ij} \alpha_{ij}} = |\mathbf{b}| \int_{\mathcal{C}} |dl_i| \int d^3r \delta^{(3)}(\mathbf{r} - \mathbf{r}'_{(l)}) = |\mathbf{b}| L, \quad (51)$$

where  $L$  is the perimeter of the dislocation loop. Thus,

$$L = \frac{1}{|\mathbf{b}|} \int d^3r \sqrt{\alpha_{ij} \alpha_{ij}}. \quad (52)$$

#### E. Direct computation of stress fields

The dislocation density tensor is calculated directly from the phase field  $\psi$  through Eq. (11). In order to find the equilibrium distortion, we numerically compute the Green's function relating the distortion  $u_{ij}$  to the dislocation density tensor  $\alpha_{ij}$  as a source. Given periodic

boundary conditions on a finite lattice, the solution can be obtained in Fourier space followed by inversion to real space (uniqueness in the determination of the distortion has been discussed in Ref. [46]; a different method may be necessary if other boundary conditions are imposed).

In Fourier space, the equations of mechanical equilibrium and incompatibility of the distortion are, respectively,

$$C_{ijkl}q_j\tilde{u}_{kl} = 0, \quad (53)$$

and

$$-\mathbf{i}\epsilon_{ilm}ql\tilde{u}_{mk} = \tilde{\alpha}_{ik}, \quad (54)$$

where  $\tilde{f}$  is the Fourier transform of  $f$  and  $\mathbf{q}$  is a general Fourier mode. To illustrate how the absence of divergence of Eq. (41) makes some of the incompatibility equations redundant, consider a tensor  $\tilde{L}_{ik}$  with the property that  $q_i\tilde{L}_{ik} = 0$ , then for e.g.,  $k = 2$ , we have

$$q_1\tilde{L}_{12} + q_2\tilde{L}_{22} + q_3\tilde{L}_{32} = 0, \quad (55)$$

which means that

$$\tilde{L}_{22} = -\frac{1}{q_2} \left( q_1\tilde{L}_{12} + q_3\tilde{L}_{32} \right). \quad (56)$$

which relates the component  $\tilde{L}_{22}$  with  $\tilde{L}_{12}$  and  $\tilde{L}_{32}$ . Thus, when Eq. (54) is satisfied for the off-diagonal components, it is satisfied for the diagonal elements identically. With this in mind, we can complete the set of equations by adding the condition of mechanical equilibrium to the diagonal equations in Eq. (54), i.e.

$$\delta_{(i)k} \frac{\mathbf{i}C_{(i)jml}}{\mu} q_j\tilde{u}_{ml} - \mathbf{i}\epsilon_{ilm}ql\tilde{u}_{mk} = \tilde{\alpha}_{ik}, \quad (57)$$

where there is no summation over  $(i)$ , and we have multiplied the elastic constant tensor by  $\mathbf{i}/\mu$  where  $\mu$  is the shear modulus of the cubic lattice, and  $C_{ijkl} = \lambda\delta_{ij}\delta_{kl} + \mu(\delta_{ik}\delta_{jl} + \delta_{il}\delta_{jk}) + \gamma\delta_{ijkl}$ . By defining  $\tilde{\mathbf{U}}$  and  $\tilde{\alpha}$  as

$$\begin{aligned} \tilde{\mathbf{U}}^T &= (u_{11}, u_{12}, u_{13}, u_{21}, u_{22}, u_{23}, u_{31}, u_{32}, u_{33}) \\ \tilde{\alpha}^T &= (\alpha_{11}, \alpha_{12}, \alpha_{13}, \alpha_{21}, \alpha_{22}, \alpha_{23}, \alpha_{31}, \alpha_{32}, \alpha_{33}), \end{aligned}$$

we rewrite Eq. (57) more compactly as

$$M(\mathbf{q})\tilde{\mathbf{U}} = \tilde{\alpha}, \quad (58)$$

where the explicit form of  $M(\mathbf{q})$  in the case of cubic anisotropy is given by

$$M(\mathbf{q}) = \mathbf{i} \begin{pmatrix} \frac{\lambda+2\mu+\gamma}{\mu}q_1 & q_2 & q_3 & q_2+q_3 & \frac{\lambda}{\mu}q_1 & 0 & -q_2+q_3 & 0 & \frac{\lambda}{\mu}q_1 \\ 0 & 0 & 0 & 0 & q_3 & 0 & 0 & -q_2 & 0 \\ 0 & 0 & 0 & 0 & 0 & q_3 & 0 & 0 & -q_2 \\ -q_3 & 0 & 0 & 0 & 0 & 0 & q_1 & 0 & 0 \\ \frac{\lambda}{\mu}q_2 & q_1-q_3 & 0 & q_1 & \frac{\lambda+2\mu+\gamma}{\mu}q_2 & q_3 & 0 & q_1+q_3 & \frac{\lambda}{\mu}q_2 \\ 0 & 0 & -q_3 & 0 & 0 & 0 & 0 & 0 & q_1 \\ q_2 & 0 & 0 & -q_1 & 0 & 0 & 0 & 0 & 0 \\ 0 & q_2 & 0 & 0 & -q_1 & 0 & 0 & 0 & 0 \\ \frac{\lambda}{\mu}q_3 & 0 & q_1+q_2 & 0 & \frac{\lambda}{\mu}q_3 & -q_1+q_2 & q_1 & q_2 & \frac{\lambda+2\mu+\gamma}{\mu}q_3 \end{pmatrix}. \quad (59)$$

$M(\mathbf{q})$  can be inverted to yield the Fourier transform of the distortion  $\tilde{\mathbf{U}}$ ,

$$\tilde{\mathbf{U}} = M^{-1}(\mathbf{q})\tilde{\alpha}. \quad (60)$$

Once  $\tilde{\mathbf{U}}$  (denoted by  $\tilde{u}_{kl}$  in components) is known, we compute the stress field in mechanical equilibrium

$$\tilde{\sigma}_{ij} = C_{ijkl}\tilde{u}_{kl}. \quad (61)$$

The dislocation density  $\alpha_{ik}$  as obtained from the phase field as in Eq. (11) has a very small divergence due to numerical round-off errors. We impose  $\partial_i\alpha_{ik} = 0$  explicitly before evaluating  $\tilde{\sigma}$ , which improves numerical stability.

## DATA AVAILABILITY

The data and the codes that support the findings of this study are available from the corresponding author upon reasonable request.

## ACKNOWLEDGEMENTS

V.S. and L.A. acknowledges support from the Research Council of Norway through the Center of Excellence

funding scheme, Project No. 262644 (PoreLab). M.S. acknowledges support from the Emmy Noether Programme of the German Research Foundation (DFG) under Grant No. SA4032/2-1. The research of J.V. is supported by the National Science Foundation, contract No. DMR-1838977.

### AUTHOR CONTRIBUTIONS

L.A. and J.V. conceived of the presented idea in Sec. II and V.S. developed the theory with the help of A.S. V.S. performed the numerical simulations of Sec. III A and derived the theoretical analysis of Sec. III B together with L.A. and M.S. V.S. developed the theoretical framework of III C-III D. All authors discussed the results and contributed to the final manuscript.

### ADDITIONAL INFORMATION

**Competing interests:** The authors declare that there are no competing interests.

### Appendix A: Inversion formula for highly symmetric lattice vector sets

In inverting Eq. (2) to obtain the displacement field  $\mathbf{u}$  in terms of the phases  $\theta_n$ , we used the result of Eq. (3). This follows from the properties of moment tensors constructed from lattice vector sets  $\mathcal{Q} = \{\mathbf{q}^{(n)}\}_{n=1}^N$ . The  $p$ -th order moment tensor constructed from  $\mathcal{Q}$  is given by

$$Q_{i_1 \dots i_p} = \sum_{n=1}^N q_{i_1}^{(n)} \dots q_{i_p}^{(n)}. \quad (\text{A1})$$

In two dimensions, for a parity-invariant lattice vector set that has a  $B$ -fold symmetry, Ref. [47] showed that all  $p$ -th order moments vanish for odd  $p$  and are isotropic for  $p < B$ . Every isotropic rank 2 tensor is proportional to the identity tensor  $\delta_{ij}$ , so for a 2D lattice vector set having four-fold symmetry, such as the set of shortest reciprocal lattice vectors  $\{\mathbf{q}^{(n)}\}_{n=1}^4$  of the square lattice, we have  $\sum_{n=1}^4 q_i^{(n)} q_j^{(n)} \propto \delta_{ij}$  (Figs. 3 and 5 in Ref. [30] show the reciprocal lattice vector sets discussed in this appendix). Taking the trace and using that the vectors have the same length  $|\mathbf{q}^{(n)}| = q_0$ , we get  $\sum_{n=1}^4 q_i^{(n)} q_j^{(n)} = 2q_0^2 \delta_{ij}$ . In general, for any 2D parity invariant lattice vector set  $\{\mathbf{q}^{(n)}\}_{n=1}^N$  with a  $B$ -fold symmetry where  $B > 2$ , we have

$$2\text{D: } \sum_{n=1}^N q_i^{(n)} q_j^{(n)} = \frac{Nq_0^2}{2} \delta_{ij}. \quad (\text{A2})$$

As mentioned, this holds for the two dimensional (2D) square lattice, but it also holds for the 2D hexagonal

lattice. In fact, the six-fold symmetry of the hexagonal lattice ensures that also every fourth-order moment tensor is isotropic, which results in elastic properties of the 2D hexagonal PFC model being isotropic [30].

To show this identity for a three dimensional (3D) parity invariant vector set with cubic symmetry, we generalize the proof in Ref. [47] to a particular case of a 3D vector set that is symmetric with respect to  $90^\circ$  rotations around each coordinate axis, such as the set of shortest reciprocal lattice vectors  $\{\mathbf{q}^{(n)}\}_{n=1}^N$  of bcc, fcc or simple cubic structures. Let  $\mathbf{v}$  be an eigenvector of  $Q_{ij}$  with eigenvalue  $\lambda$ , i.e.,  $Q_{ij} v_j = \lambda v_i$ . Since  $Q_{ij}$  is invariant under a  $90^\circ$  rotation  $R_{ij}^{(x)}$  around the  $x$ -axis, we get  $Q_{ij} R_{jl}^{(x)} v_l = \lambda R_{il}^{(x)} v_l$ , showing that  $R^{(x)} \mathbf{v}$  is also an eigenvector of  $Q_{ij}$  with the same eigenvalue  $\lambda$ . Repeating for a rotation around the  $y$ -axis demonstrates that  $Q_{ij}$  has only one eigenvalue  $\lambda$ , so that it must be proportional to the rank 2 identity tensor  $Q_{ij} \propto \delta_{ij}$ . Taking the trace and using that the vectors have the same length  $|\mathbf{q}^{(n)}| = q_0$ , we find

$$3\text{D: } \sum_{n=1}^N q_i^{(n)} q_j^{(n)} = \frac{Nq_0^2}{3} \delta_{ij}. \quad (\text{A3})$$

### Appendix B: Amplitude decoupling

When accounting for the bcc lattice symmetry through  $\mathbf{q}_n$  as in Eq. (21), the (complex) polynomial  $f^s$  entering the coarse-grained energy  $F_\eta$  defined in Eq. (24) [12, 27, 40] is

$$\begin{aligned} f^s = & -2t(\eta_1^* \eta_2 \eta_6 + \eta_1^* \eta_3 \eta_5 + \eta_2^* \eta_3 \eta_4 + \eta_4 \eta_5^* \eta_6 + \text{c.c.}) \\ & + 6v(\eta_1^* \eta_2 \eta_4^* \eta_5 + \eta_1^* \eta_3 \eta_4 \eta_6 + \eta_2^* \eta_3 \eta_5 \eta_6^* + \text{c.c.}), \end{aligned} \quad (\text{B1})$$

which gives

$$\begin{aligned} \frac{\partial f^s}{\partial \eta_1^*} &= -2t(\eta_2 \eta_6 + \eta_3 \eta_5) + 6v(\eta_2 \eta_4^* \eta_5 + \eta_3 \eta_4 \eta_6) \\ \frac{\partial f^s}{\partial \eta_2^*} &= -2t(\eta_1 \eta_6^* + \eta_3 \eta_4) + 6v(\eta_1 \eta_4 \eta_5^* + \eta_3 \eta_5 \eta_6^*) \\ \frac{\partial f^s}{\partial \eta_3^*} &= -2t(\eta_1 \eta_5^* + \eta_2 \eta_4^*) + 6v(\eta_1 \eta_4^* \eta_6^* + \eta_2 \eta_5^* \eta_6) \\ \frac{\partial f^s}{\partial \eta_4^*} &= -2t(\eta_2 \eta_3^* + \eta_5 \eta_6^*) + 6v(\eta_1^* \eta_2 \eta_5 + \eta_1 \eta_3^* \eta_6^*) \\ \frac{\partial f^s}{\partial \eta_5^*} &= -2t(\eta_1 \eta_3^* + \eta_4 \eta_6) + 6v(\eta_1 \eta_2^* \eta_4 + \eta_2 \eta_3^* \eta_6) \\ \frac{\partial f^s}{\partial \eta_6^*} &= -2t(\eta_1 \eta_2^* + \eta_4^* \eta_5) + 6v(\eta_1 \eta_3^* \eta_4^* + \eta_2^* \eta_3 \eta_5) \end{aligned} \quad (\text{B2})$$

In the equation for the dislocation velocity, Eq. (17), the only contributing amplitudes are those for which  $s_n \neq 0$ . By comparing Eqs. (B2) to the dislocation charges for the possible Burgers vector in the bcc lattice, Table I, and

noting that, at the dislocation core,  $\eta_n = 0$  for  $s_n \neq 0$ , we find

$$s_n \neq 0 : \quad \frac{\partial f^s}{\partial \eta_n} = 0. \quad (\text{B3})$$

at the dislocation core. Therefore the corresponding evolution laws defined in Eqs. (25)–(26) are fully decoupled.

- 
- [1] K. R. Elder, Mark Katakowski, Mikko Haataja, and Martin Grant. Modeling Elasticity in Crystal Growth. *Physical Review Letters*, 88(24):245701, June 2002.
  - [2] Heike Emmerich, Hartmut Löwen, Raphael Wittkowski, Thomas Gruhn, Gyula I. Tóth, György Tegze, and László Gránásy. Phase-field-crystal models for condensed matter dynamics on atomic length and diffusive time scales: An overview. *Advances in Physics*, 61(6):665–743, 2012.
  - [3] Kasra Momeni, Yanzhou Ji, Kehao Zhang, Joshua A. Robinson, and Long-Qing Chen. Multiscale framework for simulation-guided growth of 2D materials. *npj 2D Materials and Applications*, 2(1):1–7, September 2018.
  - [4] Vidar Skogvoll, Audun Skaugen, Luiza Angheluta, and Jorge Viñals. Dislocation nucleation in the phase-field crystal model. *Physical Review B*, 103(1):014107, January 2021.
  - [5] Jaber Rezaei Mianroodi and Bob Svendsen. Atomistically determined phase-field modeling of dislocation dissociation, stacking fault formation, dislocation slip, and reactions in fcc systems. *Journal of the Mechanics and Physics of Solids*, 77:109–122, April 2015.
  - [6] Joel Berry, Jörg Rottler, Chad W. Sinclair, and Nikolas Provatas. Atomistic study of diffusion-mediated plasticity and creep using phase field crystal methods. *Phys. Rev. B*, 92(13):134103, October 2015.
  - [7] Zhe-Yuan Liu, Ying-Jun Gao, Qian-Qian Deng, Yi-Xuan Li, Zong-Ji Huang, Kun Liao, and Zhi-Rong Luo. A nanoscale study of nucleation and propagation of Zener types cracks at dislocations: Phase field crystal model. *Computational Materials Science*, 179:109640, June 2020.
  - [8] N. Provatas, J. A. Dantzig, B. Athreya, P. Chan, P. Stefanovic, N. Goldenfeld, and K. R. Elder. Using the phase-field crystal method in the multi-scale modeling of microstructure evolution. *JOM*, 59(7):83–90, July 2007.
  - [9] Kuo-An Wu and Peter W. Voorhees. Phase field crystal simulations of nanocrystalline grain growth in two dimensions. *Acta Materialia*, 60(1):407–419, January 2012.
  - [10] Akinori Yamanaka, Kevin McReynolds, and Peter W. Voorhees. Phase field crystal simulation of grain boundary motion, grain rotation and dislocation reactions in a BCC bicrystal. *Acta Materialia*, 133:160–171, July 2017.
  - [11] Marco Salvalaglio, Rainer Backofen, K. R. Elder, and Axel Voigt. Defects at grain boundaries: A coarse-grained, three-dimensional description by the amplitude expansion of the phase-field crystal model. *Physical Review Materials*, 2(5):053804, May 2018.
  - [12] K. R. Elder, Zhi-Feng Huang, and Nikolas Provatas. Amplitude expansion of the binary phase-field-crystal model. *Phys. Rev. E*, 81(1):011602, January 2010.
  - [13] K. R. Elder, Nikolas Provatas, Joel Berry, Peter Stefanovic, and Martin Grant. Phase-field crystal modeling and classical density functional theory of freezing. *Physical Review B*, 75(6):064107, February 2007.
  - [14] Zhi-Feng Huang, K. R. Elder, and Nikolas Provatas. Phase-field-crystal dynamics for binary systems: Derivation from dynamical density functional theory, amplitude equation formalism, and applications to alloy heterostructures. *Physical Review E*, 82(2):021605, August 2010.
  - [15] Andrew J. Archer, Daniel J. Ratliff, Alastair M. Rucklidge, and Priya Subramanian. Deriving phase field crystal theory from dynamical density functional theory: Consequences of the approximations. *Physical Review E*, 100(2):022140, August 2019.
  - [16] S. Brazovskii. Phase transition of an isotropic system to a nonuniform state. *Soviet Journal of Experimental and Theoretical Physics*, 41:85, 1975.
  - [17] J. Swift and P. C. Hohenberg. Hydrodynamic fluctuations at the convective instability. *Physical Review A*, 15(1):319–328, January 1977.
  - [18] Amit Acharya and Jorge Viñals. Field dislocation mechanics and phase field crystal models. *Physical Review B*, 102(6):064109, August 2020.
  - [19] A. M. Kosevich. Crystal dislocations and the theory of elasticity. In F. R. N. Nabarro, editor, *Dislocations in Solids, Vol. 1*, pages 33–141. North-Holland, Amsterdam, 1979.
  - [20] Vasily Bulatov and Wei Cai. *Computer Simulations of Dislocations*. OUP Oxford, November 2006.
  - [21] Audun Skaugen, Luiza Angheluta, and Jorge Viñals. Dislocation dynamics and crystal plasticity in the phase-field crystal model. *Phys. Rev. B*, 97(5):054113, February 2018.
  - [22] Peter Stefanovic, Mikko Haataja, and Nikolas Provatas. Phase-field crystals with elastic interactions. *Phys. Rev. Lett.*, 96(22):225504, June 2006.
  - [23] J. A. P. Ramos, E. Granato, S. C. Ying, C. V. Achim, K. R. Elder, and T. Ala-Nissila. Dynamical transitions and sliding friction of the phase-field-crystal model with pinning. *Phys. Rev. E*, 81(1):011121, January 2010.
  - [24] Gyula I. Tóth, László Gránásy, and György Tegze. Non-linear hydrodynamic theory of crystallization. *Journal of Physics: Condensed Matter*, 26(5):055001, December 2013.
  - [25] V. Heinonen, C. V. Achim, J. M. Kosterlitz, See-Chen Ying, J. Lowengrub, and T. Ala-Nissila. Consistent Hydrodynamics for Phase Field Crystals. *Physical Review Letters*, 116(2):024303, January 2016.
  - [26] V. Heinonen, C. V. Achim, K. R. Elder, S. Buyukdagli, and T. Ala-Nissila. Phase-field-crystal models and mechanical equilibrium. *Phys. Rev. E*, 89(3):032411, March 2014.
  - [27] Nigel Goldenfeld, Badrinarayan P. Athreya, and Jonathan A. Dantzig. Renormalization group approach to multiscale simulation of polycrystalline materials using the phase field crystal model. *Phys. Rev. E*, 72(2):020601, August 2005.

- [28] Audun Skaugen, Luiza Angheluta, and Jorge Viñals. Separation of elastic and plastic timescales in a phase field crystal model. *Phys. Rev. Lett.*, 121(25):255501, December 2018.
- [29] Marco Salvalaglio, Luiza Angheluta, Zhi-Feng Huang, Axel Voigt, Ken R. Elder, and Jorge Viñals. A coarse-grained phase-field crystal model of plastic motion. *Journal of the Mechanics and Physics of Solids*, 137:103856, 2020.
- [30] Vidar Skogvoll, Audun Skaugen, and Luiza Angheluta. Stress in ordered systems: Ginzburg-Landau-type density field theory. *Physical Review B*, 103(22):224107, June 2021.
- [31] Wei Cai, Athanasios Arsenlis, Christopher R. Weinberger, and Vasily V. Bulatov. A non-singular continuum theory of dislocations. *Journal of the Mechanics and Physics of Solids*, 54(3):561–587, March 2006.
- [32] Markus Lazar and Gérard A. Maugin. Nonsingular stress and strain fields of dislocations and disclinations in first strain gradient elasticity. *International Journal of Engineering Science*, 43(13):1157–1184, September 2005.
- [33] Markus Lazar. Non-singular dislocation continuum theories: Strain gradient elasticity vs. Peierls–Nabarro model. *Philosophical Magazine*, 97(34):3246–3275, December 2017.
- [34] Marco Salvalaglio, Axel Voigt, and Ken R. Elder. Closing the gap between atomic-scale lattice deformations and continuum elasticity. *npj Computational Materials*, 5(1):48, 2019.
- [35] Markus Lazar. On gradient field theories: Gradient magnetostatics and gradient elasticity. *Philosophical Magazine*, 94(25):2840–2874, September 2014.
- [36] Gene F. Mazenko. Velocity distribution for strings in phase-ordering kinetics. *Physical Review E*, 59(2):1574–1584, February 1999.
- [37] Luiza Angheluta, Patricio Jeraldo, and Nigel Goldenfeld. Anisotropic velocity statistics of topological defects under shear flow. *Phys. Rev. E*, 85(1):011153, January 2012.
- [38] K. R. Elder and Martin Grant. Modeling elastic and plastic deformations in nonequilibrium processing using phase field crystals. *Phys. Rev. E*, 70(5):051605, November 2004.
- [39] Denis Boyer and Jorge Viñals. Weakly nonlinear theory of grain boundary motion in patterns with crystalline symmetry. *Phys. Rev. Lett.*, 89(5):055501, 2002.
- [40] Badrinarayan P. Athreya, Nigel Goldenfeld, and Jonathan A. Dantzig. Renormalization-group theory for the phase-field crystal equation. *Physical Review E*, 74(1):011601, July 2006.
- [41] Marco Salvalaglio, Rainer Backofen, Axel Voigt, and Ken R. Elder. Controlling the energy of defects and interfaces in the amplitude expansion of the phase-field crystal model. *Phys. Rev. E*, 96:023301, Aug 2017.
- [42] Marco Salvalaglio, Axel Voigt, Zhi-Feng Huang, and Ken R. Elder. Mesoscale Defect Motion in Binary Systems: Effects of Compositional Strain and Cottrell Atmospheres. *Physical Review Letters*, 126(18):185502, May 2021.
- [43] P. H. Dederichs and G. Leibfried. Elastic Green’s Function for Anisotropic Cubic Crystals. *Physical Review*, 188(3):1175–1183, December 1969.
- [44] Due to the geometric similarity in how the loop annihilates in the different models, there is no observable difference in the continuum elastic stress field predictions between using  $\alpha$  from either model as a source.
- [45] S. M. Cox and P. C. Matthews. Exponential Time Differencing for Stiff Systems. *Journal of Computational Physics*, 176(2):430–455, March 2002.
- [46] A. Acharya, R. J. Knops, and J. Sivaloganathan. On the structure of linear dislocation field theory. *Journal of the Mechanics and Physics of Solids*, 130:216–244, September 2019.
- [47] Hudong Chen and Steven Orszag. Moment isotropy and discrete rotational symmetry of two-dimensional lattice vectors. *Philosophical Transactions of the Royal Society A: Mathematical, Physical and Engineering Sciences*, 369(1944):2176–2183, June 2011.